SCIENCE CHINA
Information Sciences

• RESEARCH PAPER •

October 2025, Vol. 68, Iss. 10, 202403:1–202403:10
https://doi.org/10.1007/s11432-024-4360-9

Bifunctional monolithic transparent device for both neuromorphic computing and omnidirectional self-driven photodetection

Yanyan CHANG[1,2], Min JIANG[2,3], Lian JI[1*] & Yukun ZHAO[2,3*]

[1]*School of Energy Science and Engineering, Nanjing Tech University, Nanjing 211816, China*
[2]*Suzhou Institute of Nano-Tech and Nano-Bionics (SINANO), Chinese Academy of Sciences, Suzhou 215123, China*
[3]*School of Nano-Tech and Nano-Bionics, University of Science and Technology of China, Hefei 230026, China*

Received 25 September 2024/Revised 26 December 2024/Accepted 24 March 2025/Published online 23 September 2025

Abstract Owing to the inherent discrepancy between the transient photoresponse speeds of photodetectors and artificial synapses, the integration of these elements into a single monolithic device poses notable challenges. Herein, we propose a bifunctional monolithic transparent device based on lifted-off (In,Ga)N nanowires. This device not only shows omnidirectional self-driven photodetection but also effectively functions as an artificial synapse in neuromorphic computing. The proposed device exhibits persistent photoconductivity under bias voltage and fast photoresponse without bias voltage, corresponding to the operational modes of artificial synapses and self-driven photodetectors, respectively. As a photodetector, the device exhibits omnidirectional detection, particularly owing to its transparency. As an artificial synapse, the device realizes various synaptic behaviors with ultrahigh paired-pulse-facilitation index and low energy consumption. Furthermore, an artificial neural network assembled using the proposed device exhibits a pattern recognition accuracy of 92%. The findings of the present study contribute to the advancement of omnidirectional self-driven detection and efficient neuromorphic computing.

Keywords bifunctional monolithic device, 360° omnidirectional photodetector, self-driven photodetection, artificial synapse, (In,Ga)N nanowire, neural network

Citation Chang Y Y, Jiang M, Ji L, et al. Bifunctional monolithic transparent device for both neuromorphic computing and omnidirectional self-driven photodetection. Sci China Inf Sci, 2025, 68(10): 202403, https://doi.org/10.1007/s11432-024-4360-9

1 Introduction

Photodetectors have become an indispensable part of our daily lives, serving as critical optoelectronic components in modern sensing, communication, and imaging systems [1–7]. However, the detection range of traditional photodetectors is 180°, necessitating the use of multiple devices to achieve omnidirectional detection [8]. Hence, detectors with omnidirectional light detection capabilities are required for next-generation applications, which can be realized in highly transparent devices. However, because of the limitations of opaque semiconducting materials or substrates, the fabrication of photodetectors with high transparency and omnidirectional (360°) light detection remains a challenging task.

The human brain can extract and process massive data simultaneously. Inspired by the human brain, neuromorphic computing has been proposed to mimic the operation of the nervous system [9, 10], artificial synaptic devices, which can convert sensor signals into neural-like signals, hold great potential for advancing artificial intelligence and human-computer interactions [11, 12]. The integration of artificial synapses and photodetectors into a single device could significantly simplify supporting systems and greatly expand application scenarios. However, this integration faces a fundamental challenge: synaptic devices require longer times for signal processing and storage, whereas photodetectors typically show rapid light response capabilities [13, 14]. This inherent discrepancy in their light response speeds makes it highly challenging to fabricate a single monolithic device integrating the two.

GaN-based materials exhibit tunable bandgaps, non-toxicity, and low power consumption, making them highly suitable for a wide range of optoelectronic applications [15]. Compared with bulk materials,

* Corresponding author (email: jilian@njtech.edu.cn, ykzhao2017@sinano.ac.cn)

(In,Ga)N nanowires (NWs) exhibit higher surface-to-volume ratio and transparency in the visible spectrum [16–18]. In our previous studies, we successfully fabricated (In,Ga)N NWs and applied them in photodetectors [19,20]. However, to date, the integration of omnidirectional photodetection and artificial synaptic functionality into a single bifunctional device based on (In,Ga)N NWs has not been reported.

Herein, we introduce a bifunctional monolithic transparent device that utilizes lifted-off (In,Ga)N NWs to realize both neuromorphic computing and omnidirectional self-driven photodetection. The device switches between these two modes through the modulation of the bias voltage, exhibiting persistent photoconductivity (PPC) and a rapid photoresponse. To evaluate the neuromorphic computing capabilities of the device, we constructed an artificial neural network for visual pattern recognition. By overcoming the technical difficulties of the integration of a photodetector with a synaptic device, the proposed device is expected to promote the development of intelligent neuromorphic computing and self-driven photodetection.

2 Experiments and methods

2.1 Preparation of (In,Ga)N NWs

To prepare materials required for the fabrication of the bifunctional device shown in Figure 1(a), (In,Ga)N NWs were grown on an n-type Si (111) substrate using a Veeco GEN20A molecular beam epitaxy system. This instrument is equipped with Al, Ga, and In effusion cells, and an N plasma source. Prior to NW growth, the Si substrate was heated to approximately 900°C for 15 min in the growth chamber to remove the surface oxide layer. After that, an AlN sacrificial layer with a thickness of 3 nm was grown at 830°C on the substrate. Subsequently, bottom GaN NWs were grown for 70 min at a Ga flux of approximately 4.0×10^{-8} Torr. Then, the substrate temperature was reduced to 630°C for the growth of (In,Ga)N segments, performed at an In/Ga flux ratio of 1.0. During the growth process, the sample was rotated at a speed of 120°/s to improve the uniformity of the NWs.

2.2 Fabrication procedure of bifunctional device

To prepare the transparent device, the opaque Si substrate had to be removed. The first step involved cutting the grown sample into small slices. Next, the sacrificial AlN layer was electrochemically etched in a 2 mol/L HNO_3 solution to detach the NWs from the Si substrate (Figures A1(a) and (b)). Electrochemical etching was performed using an H-cell setup. As shown in Figure A1(c), the lifted-off NWs were transferred onto ITO glass, which served as the bottom electrode of the device. Subsequently, a 400-nm SiO_2 layer was deposited on the upper surface of the NWs via chemical vapor deposition. A region of the SiO_2 layer was then removed through lithography and reactive ion etching to expose a portion of the (In,Ga)N NWs (Figure A1(d)). Subsequently, a patterned Ag electrode was attached to the SiO_2 layer (Figure A1(e)). Finally, a piece of graphene was transferred onto the sample, completing device fabrication (Figure A1(f)). The effective light-receiving area of the device was 0.1256 cm^2.

2.3 Characterization and measurements

The NWs were observed using scanning electron microscopy (SEM; S-4800, HITACHI) at 3 kV. Spherical aberration-corrected scanning transmission electron microscopy (AC-STEM; Themis Z, FEI) was employed to characterize the morphologies, elemental distribution, and atomic arrangement of the NWs, which were prepared by focused ion beam (Scios, FEI). The chemical states and atomic binding were characterized through X-ray photoelectron spectroscopy (XPS). The transmittance of the device was measured using spectrophotometry (LAMBDA 750). A room-temperature photoluminescence test was performed using a 325 nm laser (LABRAM HR).

3 Results and discussion

3.1 Design of bifunctional monolithic transparent device

The synaptic device exhibits PPC under bias, but the photocurrent of the photodetector quickly returns to the initial value in the absence of bias. This implies that the bifunctional device should demonstrate two distinct photoresponse states under different conditions (Figure 1(a)). At the bias voltage of

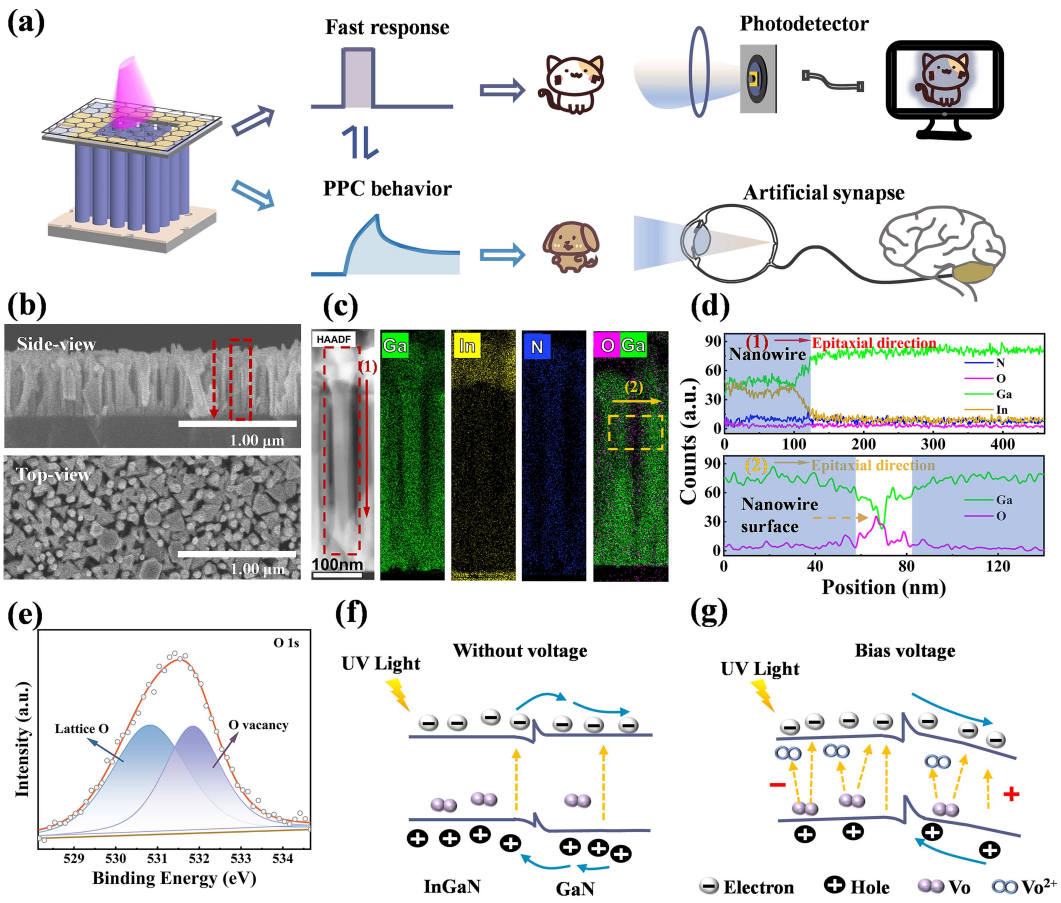

Figure 1 (Color online) (a) Schematic of the bifunctional device exhibiting photodetector and artificial synapse functionalities. (b) Top-view and side-view SEM images of vertical (In,Ga)N NWs. (c) Side-view AC-STEM image of an (In,Ga)N NW. The white scale bar represents 100 nm. (d) High-resolution energy dispersive X-ray elemental maps of the (In,Ga)N NW. (1) and (2) regions in (d) correspond to those in (c). (e) O 1s XPS spectra of (In,Ga)N NWs. Energy-band diagrams of heterostructure under illumination (f) without and (g) with applied bias voltage.

0 V, the photovoltaic effect of the (In,Ga)N/GaN heterojunction produces a rapid photoresponse under illumination, enabling self-driven functionality. At the same time, under bias voltage and ultraviolet illumination, carriers are effectively separated and then injected into oxygen vacancies, causing their ionization and positive charging, thereby inducing the PPC effect (synaptic plasticity) [21–23].

The dense (In,Ga)N NWs (Figure 1(b)) are vertically aligned and have a height of ∼600 nm. Figures 1(c) and (d) show the presence of In in the upper segment of NWs, which is consistent with the device design. Additionally, Figure 1(d) reveals the presence of O on the NW surface. As the photoluminescence spectrum features a peak at ∼590 nm (Figure A2), the In content was estimated at ∼36% according to the Vegard law [15]. The XPS spectrum in Figure 1(e) shows the presence of oxygen vacancies (Vo) on the NW surface. These vacancies could be the primary factor triggering the PPC effect [24, 25]. To investigate carrier transport, energy-band diagrams were plotted (Figures 1(f) and (g)). When the (In,Ga)N/GaN heterojunction is illuminated with 365 nm light (Figures 1(f) and (g)), both (In,Ga)N and GaN absorb photons, resulting in the excitation photogenerated carriers-electrons and holes [26]. These photogenerated carriers are separated owing to the internal electric field in the (In,Ga)N/GaN heterojunction, thereby generating photocurrent and producing a significant photovoltaic effect [27–29]. This behavior could contribute to the self-driven functionality of the device. At the same time, under 365 nm illumination and an electric field, Vo in both (In,Ga)N and GaN undergo ionization (Figure 1(g)), producing electrons and ionized oxygen vacancies (Vo^{2+}). Guided by the electric field, these electrons migrate toward the heterointerface, thereby reducing the energy barrier and weakening the photocurrent response [30, 31]. After illumination, Vo^{2+} and electrons do not immediately recombine [32]. Consequently, the device exhibits gradual photocurrent decay, making it suitable for use as a synaptic device. Hence, the functionality of the monolithic device can be effectively switched between a

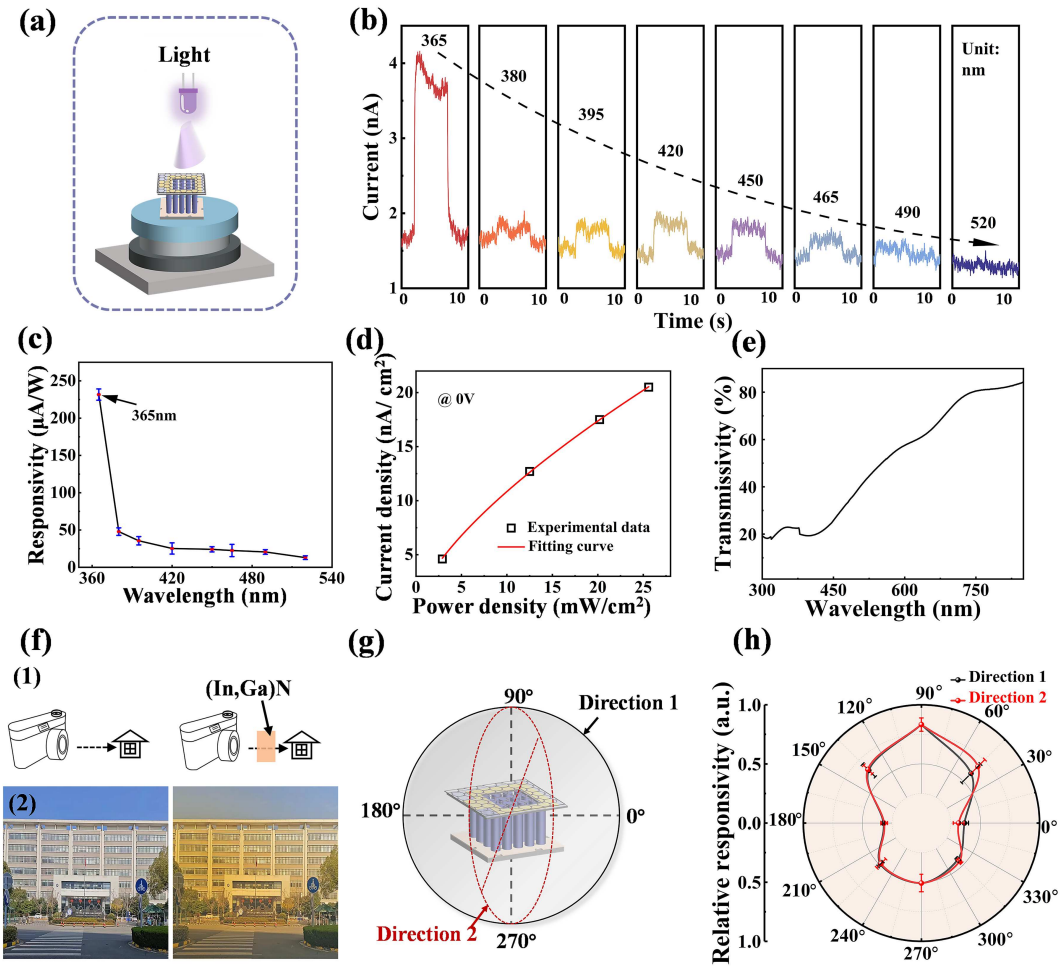

Figure 2 (Color online) (a) Schematic of the bifunctional device operating as a photodetector at 0 V. (b) The transient photoresponse curves of the device under incident light of various wavelengths. (c) Responsivity of the photodetector under different wavelengths of incident light. (d) Current density as a function of incident light intensity. (e) Transmissivity of the lifted-off (In,Ga)N NWs. (f) (1) Image capture through the lifted-off (In,Ga)N NWs. (2) Left image: a photograph of the object. Right image: a photograph captured through the lifted-off (In,Ga)N NWs. (g) Schematic of the method used to investigate omnidirectional detection. (h) Relative responsivity of the omnidirectional photodetector with different rotation angles along Direction 1 and Direction 2.

photodetector and a synaptic device through the application of bias voltage.

3.2 360° omnidirectional detection

To assess the performance of the device in the detector mode (Figure 2(a)), we measured the transient photoresponse curves and responsivity of the device under incident light of various wavelengths at 0 V (Figure 2(b)). The response current at 365 nm was measured under an incident light intensity of 25.6 mW/cm^2. The responsivity (R) was calculated as the follows [33–35]:

$$I_{\rm ph} = I_{\rm light} - I_{\rm dark}, \tag{1}$$

$$J_{\rm ph} = I_{\rm ph}/S, \tag{2}$$

$$R = J_{\rm ph}/P_{\rm inc}, \tag{3}$$

where $I_{\rm light}$ and $I_{\rm dark}$ represent the current with and without irradiation, respectively; $I_{\rm ph}$ is photocurrent, $J_{\rm ph}$ is the photocurrent density; S is the effective area of the device (0.1256 cm^2); and $P_{\rm inc}$ is the incident light intensity. To ensure measurement accuracy, each responsivity was measured three times. Figure 2(c) shows the average photoresponsivities with the corresponding error bars. The highest responsivity is 233 μA/W at 365 nm. As shown in Figure A3, the photocurrent density increases with the incident

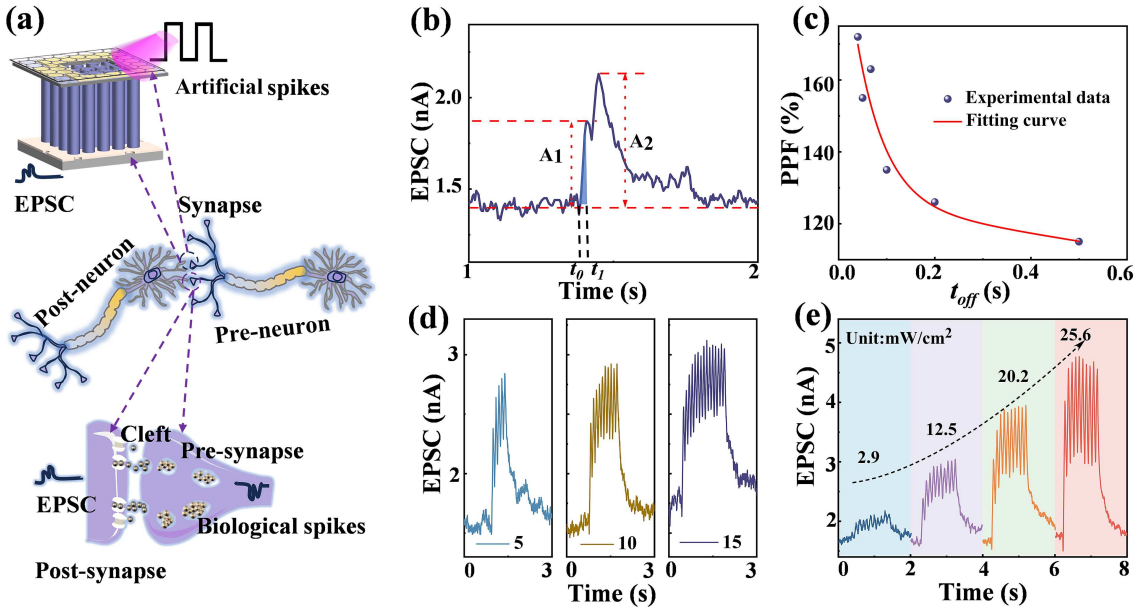

Figure 3 (Color online) (a) Schematic of the bifunctional device acting as the biological synapse. (b) EPSC of the synaptic device under illumination with two consecutive light pulses. (c) PPF index as a function of the light pulse interval (t_{off}). EPSC of the synaptic device under illumination of (d) different numbers and (e) different densities of light pulses. The light wavelength is 365 nm.

light intensity. The relationship between the steady-state photocurrent and the incident light intensity was fitted using the following equation (Figure 2(d)) [33,36]:

$$J_{\text{ph}}\alpha P_{\text{inc}}^{\alpha}, \tag{4}$$

where α is a factor determining the photocurrent response to light intensity; J_{ph} is the photocurrent density; and P_{inc} is the incident light intensity. The fitted α value for this device is 0.68, which is close to the ideal value. With the increase in light intensity, the photocurrent density gradually saturates. Transparency is an important parameter of photodetectors because the invisibility or quasi-invisibility of the detector can provide many novel functionalities [17, 37]. The lifted-off (In,Ga)N NWs exhibit remarkable transmittance in the visible range, with the maximum transmissivity exceeding 80% (Figure 2(e)). To visually illustrate the transparency of the prepared (In,Ga)N NWs, we took photographs through them (Figure 2(f)). High transparency enables the photodetector to exhibit omnidirectional detection, that is, to detect light from all angles [36, 38]. To illustrate this capability, we measured the response of the device to incident light from different angles. In Figure 2(g), "Direction 1" and "Direction 2" are two perpendicular detection paths. The responsivity was measured thrice every 45°. Figure 2(h) presents the average responsivity at each angle, along with the corresponding error bars. The responsivity initially increases with the increase in incidence angle from 0° to 90° and decreases to the initial value with the further increase in angle to 180°. Notably, the responsivity trend in the rear 180° mirrors that in the front 180°. This angle-dependent photoresponse is invaluable for the swift determination of the direction of incident light.

3.3 Synaptic device and neuromorphic computing

In biological neural networks, synapses comprising presynaptic membranes, synaptic clefts, and postsynaptic membranes facilitate information transmission between adjacent neurons (Figure 3(a)) [39]. Upon the stimulation of the presynaptic neuron, the presynaptic membrane releases neurotransmitters into the synaptic cleft [40, 41]. These neurotransmitters then diffuse toward the postsynaptic membrane and bind to receptors, triggering excitatory postsynaptic current (EPSC). Neurotransmitters play a role in information transmission, and the magnitude of EPSC is governed by the synaptic weight [42]. This mechanism is fundamental for the transmission, processing, and storage of information within the biological nervous system, serving as a cornerstone of synaptic function [43–45]. Our bifunctional device was used to imitate the operation of biological synapses, with the transport of photogenerated carriers

under illumination simulating the transport of neurotransmitters in biological neural networks. Based on the PPC behavior exhibited by the device when a 2 V bias voltage is applied, we systematically investigate its performance as an artificial synapse. Paired pulse facilitation (PPF) refers to the phenomenon where the EPSC excited by the second pulse is greater than that of the first pulse, which is a typical behavior of short-term plasticity (STP) [46]. Figure 3(b) shows the EPSC phenomenon induced by a pair of continuous light pulses with an interval of 0.05 s. The peak of EPSC responding to the second pulse (A_2) is significantly greater than that responding to the first pulse (A_1), indicating the typical PPF phenomenon. This is because the carriers generated by the first light pulse have not been fully collected by the electrode before the arrival of the second light pulse, resulting in more carriers in the device when the second light pulse is applied. The PPF index ($Q_{\rm PPF}$) is used to quantify the PPF behavior, which is defined as follows [47]:

$$Q_{\rm PPF} = A_2/A_1, \tag{5}$$

$$Q_{\rm PPF} = C_1 \exp\left(-\frac{\tau_{\rm off}}{\tau_1}\right) + C_2 \exp\left(-\frac{\tau_{\rm off}}{\tau_2}\right) + y_0, \tag{6}$$

where τ_1 and τ_2 are the characteristic relaxation times for fast and slow processes, respectively, and C_1 and C_2 are their facilitation amplitudes, respectively [48]. As the critical value increases from 0.04 to 0.5 s, the PPF index value decreases from 172% to 115% (Figure 3(c)). Using (6), the values of τ_1 and τ_2 are derived to be 0.06 and 5.25 s, respectively, corresponding to fast and slow decay processes. The difference between slow and fast PPF decay can be considered as biological synaptic connectivity enhancement [49–51]. Thus, artificial synaptic devices based on (In,Ga)N NWs have the ability to mimic biological synapses. In the field of brain-like devices, energy consumption (E) is a crucial parameter, and its specific calculation is based on the following equation [52]:

$$E = I_{\rm peak} \times V \times t_d = \int_{t_0}^{t_1} V \cdot I(t){\rm d}t, \tag{7}$$

where $I_{\rm peak}$ is the maximum EPSC, and V is the bias voltage (2 V); time points t_0 and t_1 represent the beginning and end of the light irradiation, respectively; the duration (t_d) between t_0 and t_1 is the pulse length (0.5 s); and I is the current generated in response to light irradiation. Calculations yield the energy consumption of only 9.52×10^{-12} J under light irradiation (Figure 3(b)). As summarized in Table 1 [13, 20, 53–65], the fabricated device exhibits excellent synaptic performance, with a high PPF and low energy consumption compared to previously reported synaptic devices based on GaN and other materials. In biological neural networks, repeated synaptic stimulation leads to an increase in synaptic weight, causing a transition from short-term plasticity to long-term plasticity [30, 66]. As the number of light pulses increases, the photocurrent progressively decays, stabilizing at a higher level relative to the initial state (Figure 3(d)). Similarly, an increase in the light intensity amplifies the photocurrent response and extends its decay (Figure 3(e)). To further analyze the decay patterns, we combined the curves in Figures 3(d) and (e) (Figures A4(a) and (b)). The resulting graphs show slower decay at a greater number of light pulses or higher illumination intensity. Consequently, synaptic memory levels in the proposed device can be modulated by adjusting the frequency and intensity of light pulses, thereby simulating both short-term plasticity and long-term plasticity.

To assess its practical applicability, we used the bifunctional device to simulate the neural network using instructions in NeuroSimV3.0.58 for pattern recognition (Figure 4(a)). The neural network employs a three-layer perceptual neural model, utilizing supervised learning with backpropagation and stochastic gradient descent algorithms [14]. Handwritten numbers were obtained from the Modified National Institute of Standards and Technology (MNIST) database and divided into 28 × 28 pixels, corresponding to 784 input neurons [42]. The hidden layer comprised 100 neurons, and the output layer contained 10 neurons representing numbers 0 to 9 [67]. As shown in Figure 4(b), simulated memristors were used as synaptic weights in the neural network. Pattern recognition was performed by adjusting these synaptic weights within the memristor array. Through computation, these synaptic weights are ultimately preserved. They are determined based on the conductance data of various enhancement and inhibition states (Figure 4(c)) using the following equations:

$$G_{\rm LTP} = B\left(1 - {\rm e}^{(-\frac{P}{A})}\right) + G_{\rm min}, \tag{8}$$

$$G_{\rm LTD} = -B\left(1 - {\rm e}^{(\frac{P-P_{\rm max}}{A})}\right) + G_{\rm max}, \tag{9}$$

Table 1 Energy consumption comparison among this work and some other recently reported synaptic devices.

Materials	PPF index (%)	Energy consumption (pJ)	Dual functions	Ref.
(In,Ga)N/GaN NWs	172	9.52	Yes	This work
(Al,Ga)N NWs	166	0.558	–	[53]
GaN NWs	150	2.72	–	[54]
Si-doped/GaN	160	33.4	–	[55]
GaN MWs	108	500	–	[56]
GaN/Ga_2O_3	144	584	Yes	[13]
GaN NWs	130	300000	–	[57]
(Al,Ga)N NWs	202	2600000	–	[20]
GaN/α-In_2Se_3	115	–	–	[58]
OIHP/(Al,Ga)N	160	–	–	[59]
MoS_2/h-BN	160	28	–	[60]
CNTs	165	–	Yes	[61]
In_2O_3/ZnO	145	70000	–	[62]
ZTO	136	–	–	[63]
MoS_2/SiO_2	190	66.5	–	[64]
AlO_x	190	361	Yes	[65]

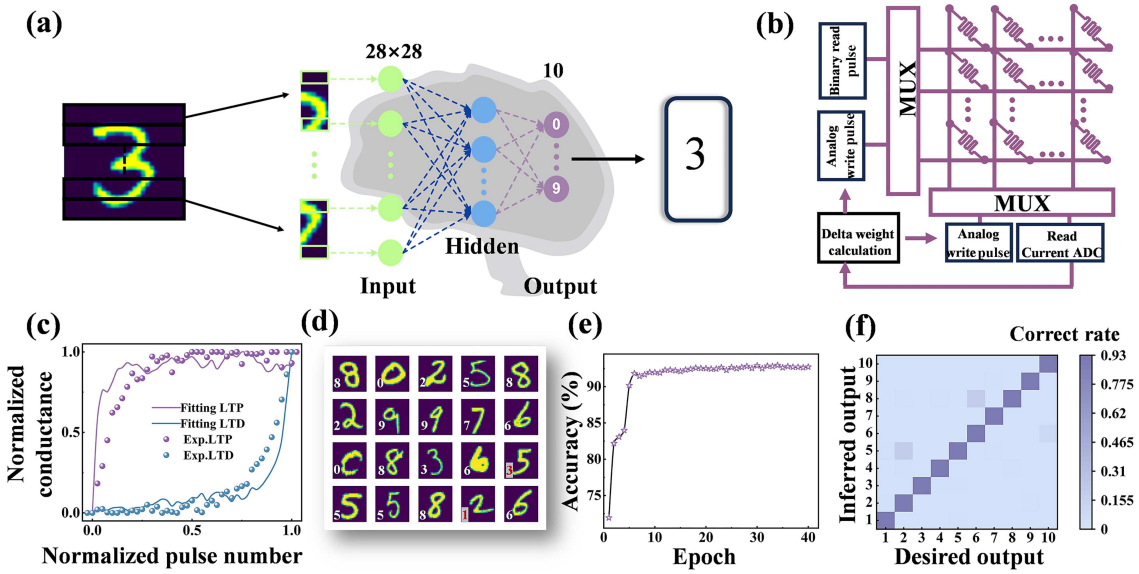

Figure 4 (Color online) (a) Schematic of pattern recognition using an artificial neural network with 784 × 100 × 10 elements; (b) block diagram of the circuit implemented using hardware; (c) the experimental data and fitted curves of LTP/LTD characteristics triggered by light pulses; (d) recognition results of the randomly selected handwritten digits from the MNIST database; (e) recognition accuracy as a function of training epoch; (f) confusion matrix for the artificial synapse after 40 training epochs.

$$B = \frac{G_{\max} - G_{\min}}{1 - \mathrm{e}^{(\frac{-P_{\max}}{A})}}, \tag{10}$$

$$G_{\text{norm}} = \frac{G_n - G_{\min}}{G_{\max} - G_{\min}}, \tag{11}$$

where G_{LTP} and G_{LTD} represent conductance values corresponding to long-term potentiation (LTP) and long-term depression (LTD), respectively. The data for LTP and LTD are presented in Figure A5. $G_{\max}$, $G_{\min}$, and $P_{\max}$ are the maximum conductivity, minimum conductivity, and the corresponding number of pulses, respectively, derived from experimental data. Parameter A regulates the weighting of nonlinear behavior. G_{norm} represents the conductance value after normalization, and G_n denotes the conductance value in the current state [43,51]. Herein, $P_{\max}$ is 40. In Figure 4(c), the value of A in the fitted curve for LTP is 0.12, and in that for LTD is -0.14. B is a function of the fitted A, comprising 1.0002 in the fitted curve for LTP and -7.9×10^{-4} in that for LTD. Simulated artificial neural network learning was executed using the MNIST database (Figure 4(d)), with 20 samples randomly selected. The majority of numbers could be accurately recognized. Figure 4(e) shows the recognition results for 10000

samples. The recognition rate of the simulated network reaches 92% after 40 training sessions. After 5 training sessions, the recognition rate is over 90%. According to the confusion matrix in Figure 4(f), the recognition accuracy remains in the range between 90.5% and 92.5%, indicating excellent stability. Leveraging the low-power demand of synaptic devices, the reduction in the number of training sessions can notably reduce energy consumption during supervised learning.

4 Conclusion

Herein, we developed a transparent device integrating omnidirectional photodetection and synaptic functionalities based on lifted-off (In,Ga)N NWs. The functionality of this device could be switched by modulating the bias voltage. In the absence of bias voltage, the bifunctional monolithic device functioned as a self-driven photodetector because of the photovoltaic effect of the (In,Ga)N/GaN heterojunction under illumination. The combined stimulation with bias voltage and illumination promoted the ionization of Vo into Vo^{2+} in the NWs, leading to PPC and thereby enabling the device to exhibit synaptic behavior. The device was used to simulate an artificial neural network, showing >92% accuracy in handwritten digit recognition. Therefore, the proposed integration strategy and the fabricated device are expected to contribute to the advancement of multifunctional devices, such as next-generation photodetectors and artificial synapses, with potential applications in communication and artificial intelligence.

Acknowledgements This work was supported by Key Research Program of Frontier Sciences, CAS (Grant No. ZDBS-LY-JSC034), National Natural Science Foundation of China (Grant No. 62174172), Basic Research Pilot Project of Suzhou (Grant No. SSD2024003), Guangdong Basic and Applied Basic Research Foundation (Grant No. 2025A1515012907), Science and Technology Youth Talent Support Project of Jiangsu Province (Grant No. JSTJ-2024-016), CIE-Smartchip Research Fund (Grant No. 2024-03), and Students' Innovation and Entrepreneurship Foundation of USTC (Grant Nos. CY2024X002B, CY2024X003B). The authors are thankful for the technical support from Nano-X, Platform for Characterization and Test and Characterization & Test platform of SINANO, CAS.

Supporting information Appendixes A–D. The supporting information is available online at info.scichina.com and link.springer.com. The supporting materials are published as submitted, without typesetting or editing. The responsibility for scientific accuracy and content remains entirely with the authors.

References

1 Wang F, Zhang T, Xie R, et al. Next-generation photodetectors beyond van der Waals junctions. Adv Mater, 2024, 36: 2301197
2 Lee K J, Wei R, Wang Y, et al. Gigantic suppression of recombination rate in 3D lead-halide perovskites for enhanced photodetector performance. Nat Photon, 2023, 17: 236–243
3 Zhang Q, Li N, Zhang T, et al. Enhanced gain and detectivity of unipolar barrier solar blind avalanche photodetector via lattice and band engineering. Nat Commun, 2023, 14: 418
4 Zhang Y, Shen W, Wu S, et al. High-speed transition-metal dichalcogenides based Schottky photodiodes for visible and infrared light communication. ACS Nano, 2022, 16: 19187–19198
5 Zhang X L, Li J, Leng B, et al. High-performance ultraviolet-visible photodetector with high sensitivity and fast response speed based on MoS_2-on-ZnO photogating heterojunction. Tungsten, 2023, 5: 91–99
6 Dai M, Chen H, Wang F, et al. Robust piezo-phototronic effect in multilayer γ-inse for high-performance self-powered flexible photodetectors. ACS Nano, 2019, 13: 7291–7299
7 Nguyen T M H, Shin S G, Choi H W, et al. Recent advances in self-powered and flexible UVC photodetectors. Exploration, 2022, 2: 20210078
8 Song W, Chen J, Li Z, et al. Self-powered MXene/GaN van der Waals heterojunction ultraviolet photodiodes with superhigh efficiency and stable current outputs. Adv Mater, 2021, 33: 2101059
9 Chen K T, Shih L C, Mao S C, et al. Mimicking pain-perceptual sensitization and pattern recognition based on capacitance- and conductance-regulated neuroplasticity in neural network. ACS Appl Mater Interfaces, 2023, 15: 9593–9603
10 Saleem A, Kumar D, Wu F, et al. An opto-electronic HFO_x-based transparent memristive synapse for neuromorphic computing system. IEEE Trans Electron Dev, 2023, 70: 1351–1358
11 Mburu M M, Lu K T, Prine N L, et al. Conjugated polymer-wrapped single-wall carbon nanotubes for high-mobility photonic/electrical fully modulated synaptic transistor. Adv Mater Technol, 2022, 7: 2101506
12 Monalisha P, Li S, Jin T, et al. Synaptic plasticity investigation in permalloy based channel material for neuromorphic computing. J Phys D-Appl Phys, 2022, 56: 015302
13 Feng S, Li J, Feng L, et al. Dual-mode conversion of photodetector and neuromorphic vision sensor via bias voltage regulation on a single device. Adv Mater, 2023, 35: 2308090
14 Han C, Han X, Han J, et al. Light-stimulated synaptic transistor with high PPF feature for artificial visual perception system application. Adv Funct Mater, 2022, 32: 2113053

15 Zhang J, Zhou M, Wu D, et al. Dual-wavelength visible photodetector based on vertical (In,Ga)N nanowires grown by molecular beam epitaxy. RSC Adv, 2021, 11: 15632–15638

16 Jeong J, Wang Q, Cha J, et al. Remote heteroepitaxy of GaN microrod heterostructures for deformable light-emitting diodes and wafer recycle. Sci Adv, 2020, 6: eaaz5180

17 Xing Z, Zhao Y, Bian L, et al. Economically detaching transparent and flexible (Al,Ga)N nanowire films with improved photoelectric response in view of ultraviolet photodetectors. Mater Adv, 2021, 2: 1006–1015

18 Zhao Y, Xing Z, Geelhaar L, et al. Detaching (In,Ga)N nanowire films for devices requiring high flexibility and transmittance. ACS Appl Nano Mater, 2020, 3: 9943–9950

19 Zhang J, Jiao B, Dai J, et al. Enhance the responsivity and response speed of self-powered ultraviolet photodetector by GaN/$CsPbBr_3$ core-shell nanowire heterojunction and hydrogel. Nano Energy, 2022, 100: 107437

20 Zhou M, Zhao Y, Gu X, et al. Realize low-power artificial photonic synapse based on (Al,Ga)N nanowire/graphene heterojunction for neuromorphic computing. APL Photon, 2023, 8: 076107

21 Esmaeili-Rad M R, Sazonov A, Nathan A. Absence of defect state creation in nanocrystalline silicon thin film transistors deduced from constant current stress measurements. Appl Phys Lett, 2007, 91: 113511

22 Lee D H, Kawamura K, Nomura K, et al. Large photoresponse in amorphous In-Ga-Zn-O and origin of reversible and slow decay. Electrochem Solid-State Lett, 2010, 13: H324

23 Powell M J, van Berkel C, Hughes J R. Time and temperature dependence of instability mechanisms in amorphous silicon thin-film transistors. Appl Phys Lett, 1989, 54: 1323–1325

24 Lim T, Lee S, Lee J, et al. Artificial synapse based on oxygen vacancy migration in ferroelectric-like C-axis-aligned crystalline InGaSnO semiconductor thin-film transistors for highly integrated neuromorphic electronics. Adv Funct Mater, 2023, 33: 2212367

25 Wang J, Zhuge F. Memristive synapses for brain-inspired computing. Adv Mater Technol, 2019, 4: 1800544

26 Jiang M, Zhao Y, Bian L, et al. Realizing bidirectional photocurrent in monolithic dual mode device for neuromorphic vision and logically encrypted transmission. Adv Funct Mater, 2024, 2416288

27 Pan X, Deng R, Hong H, et al. Sign reversal of visible to UV photocurrent in core-shell n-InGaN/p-GaN nanowire photodetectors. J Appl Phys, 2024, 136: 034501

28 Wu C, Wu F, Ma C, et al. A general strategy to ultrasensitive Ga_2O_3 based self-powered solar-blind photodetectors. Mater Today Phys, 2022, 23: 100643

29 Al-Hardan N H, Hamid M A A, Jalar A, et al. Unleashing the potential of gallium oxide: a paradigm shift in optoelectronic applications for image sensing and neuromorphic computing applications. Mater Today Phys, 2023, 38: 101279

30 Guo F, Liu Y, Zhang M, et al. A dual-functional integration of photodetectors and artificial optoelectronic synapses on a VO_2/WO_3 heterojunction device. Small Methods, 2025, 9: 2400779

31 Yang L, Singh M, Shen S W, et al. Transparent and flexible inorganic perovskite photonic artificial synapses with dual-mode operation. Adv Funct Mater, 2021, 31: 2008259

32 Hu L, Yang J, Wang J, et al. All-optically controlled memristor for optoelectronic neuromorphic computing. Adv Funct Mater, 2021, 31: 2005582

33 Li J, Xi X, Lin S, et al. Ultrahigh sensitivity graphene/nanoporous gan ultraviolet photodetectors. ACS Appl Mater Interfaces, 2020, 12: 11965–11971

34 Wang D, Huang C, Liu X, et al. Highly uniform, self-assembled AlGaN nanowires for self-powered solar-blind photodetector with fast-response speed and high responsivity. Adv Opt Mater, 2021, 9: 2000893

35 Zhang Y, Xu Y, Guo J, et al. Designing of 0D/2D mixed-dimensional van der Waals heterojunction over ultrathin g-C_3N_4 for high-performance flexible self-powered photodetector. Chem Eng J, 2021, 420: 129556

36 Fang H, Zheng C, Wu L, et al. Solution-processed self-powered transparent ultraviolet photodetectors with ultrafast response speed for high-performance communication system. Adv Funct Mater, 2019, 29: 1809013

37 Zhang X G, Sun Y L, Yu Q, et al. Smart doppler cloak operating in broad band and full polarizations. Adv Mater, 2021, 33: 2007966

38 Lien D H, Wang H P, Chen S B, et al. 360 omnidirectional, printable and transparent photodetectors for flexible optoelectronics. npj Flex Electron, 2018, 2: 19

39 Zhang Y, Liu L, Tu B, et al. An artificial synapse based on molecular junctions. Nat Commun, 2023, 14: 247

40 Lee Y J, Choi E S, Baek J H, et al. Memristive artificial synapses based on brownmillerite for endurable weight modulation. Small, 2025, 21: 2405749

41 Li R, Yue Z, Luan H, et al. Multimodal artificial synapses for neuromorphic application. Research, 2024, 7: 0427

42 Ahmed T, Tahir M, Low M X, et al. Fully light-controlled memory and neuromorphic computation in layered black phosphorus. Adv Mater, 2021, 33: 2004207

43 Dai X, Hua Q, Jiang C, et al. Artificial synapse based on a tri-layer AlN/AlScN/AlN stacked memristor for neuromorphic computing. Nano Energy, 2024, 124: 109473

44 Dong S, Liu H, Wang Y, et al. Ferroelectricity-defects synergistic artificial synapses for high recognition accuracy neuromorphic computing. ACS Appl Mater Interfaces, 2024, 16: 19235–19246

45 He Y, Xu Q, Dong X, et al. The discovery of a high-mobility two-dimensional bismuth oxyselenide semiconductor and its application in nonvolatile neuromorphic devices. ACS Nano, 2023, 17: 10783–10791

46 Kai C, Wang Y, Liu X, et al. AlGaN/GaN-based optoelectronic synaptic devices for neuromorphic computing. Adv Opt Mater, 2023, 11: 2202105

47 Mahata C, Park J, Ismail M, et al. Demonstration of electronic and optical synaptic properties modulation of reactively sputtered zinc-oxide-based artificial synapses. J Alloys Compd, 2023, 938: 168539

48 Rao T S, Kundu S, Bannur B, et al. Emulating Ebbinghaus forgetting behavior in a neuromorphic device based on 1D supramolecular nanofibres. Nanoscale, 2023, 15: 7450–7459

49 Kwon S M, Cho S W, Kim M, et al. Environment-adaptable artificial visual perception behaviors using a light-adjustable optoelectronic neuromorphic device array. Adv Mater, 2019, 31: 1906433

50 Kumar D, Li H, Das U K, et al. Flexible solution-processable black-phosphorus-based optoelectronic memristive synapses for neuromorphic computing and artificial visual perception applications. Adv Mater, 2023, 35: 2300446

51 Xie P, Huang Y, Wang W, et al. Ferroelectric P(VDF-TrFE) wrapped InGaAs nanowires for ultralow-power artificial synapses. Nano Energy, 2022, 91: 106654

52 Chen J, Ouyang W, Yang W, et al. Recent progress of heterojunction ultraviolet photodetectors: materials, integrations, and applications. Adv Funct Mater, 2020, 30: 1909909

53 Gu X, Zhou M, Zhao Y, et al. Realize ultralow-energy-consumption photo-synaptic device based on a single (Al,Ga)N nanowire for neuromorphic computing. Nano Res, 2024, 17: 1933–1941

54 Zhou M, Zhao Y, Gu X, et al. Light-stimulated low-power artificial synapse based on a single GaN nanowire for neuromorphic computing. Photon Res, 2023, 11: 1667–1677

55 Mo Y, Luo B, Dong H, et al. Light-stimulated artificial synapses based on Si-doped GaN thin films. J Mater Chem C, 2022, 10: 13099–13106

56 Hua Q, Cui X, Liu H, et al. Piezotronic synapse based on a single GaN microwire for artificial sensory systems. Nano Lett, 2020, 20: 3761–3768

57 Huang C H, Wu C Y, Lin Y F, et al. Wet-etching-boosted charge storage in 1D nitride-based systems for imitating biological synaptic behaviors. Adv Funct Mater, 2023, 33: 2306030

58 Yang J Y, Park M, Yeom M J, et al. Reconfigurable physical reservoir in GaN/α-In_2Se_3 HEMTs enabled by out-of-plane local polarization of ferroelectric 2D layer. ACS Nano, 2023, 17: 7695–7704

59 Hong X, Huang Y, Tian Q, et al. Two-dimensional perovskite-gated AlGaN/GaN high-electron-mobility-transistor for neuromorphic vision sensor. Adv Sci, 2022, 9: 2202019

60 Pan X, Zheng Y, Shi Y, et al. Surface charge transfer doping enabled large hysteresis in van der Waals heterostructures for artificial synapse. ACS Mater Lett, 2021, 3: 235–242

61 Dong L, Xue B, Wei G, et al. Highly promising 2D/1D BP-C/CNT bionic opto-olfactory co-sensory artificial synapses for multisensory integration. Adv Sci, 2024, 11: 2403665

62 Liu Q, Yin L, Zhao C, et al. All-in-one metal-oxide heterojunction artificial synapses for visual sensory and neuromorphic computing systems. Nano Energy, 2022, 97: 107171

63 Qu S, Sun L, Zhang S, et al. An artificially-intelligent cornea with tactile sensation enables sensory expansion and interaction. Nat Commun, 2023, 14: 7181

64 Huang M, Ali W, Yang L, et al. Multifunctional optoelectronic synapses based on arrayed MoS_2 monolayers emulating human association memory. Adv Sci, 2023, 10: 2300120

65 Wang X, Yang S, Qin Z, et al. Enhanced multiwavelength response of flexible synaptic transistors for human sunburned skin simulation and neuromorphic computation. Adv Mater, 2023, 35: 2303699

66 Hao D D, Yang D, Liang H X, et al. Lead-free perovskites-based photonic synaptic devices with zero electric energy consumption. Sci China Inf Sci, 2024, 67: 162401

67 Shen C, Gao X, Chen C, et al. ZnO nanowire optoelectronic synapse for neuromorphic computing. Nanotechnology, 2021, 33: 065205